Quantum posts with tailored structural properties, electronic and optical properties for opto- and quantum electronic device applications

H. J. Krenner

Materials Department, University of California, Santa Barbara CA 93106, USA

Lehrstuhl für Experimentalphysik 1, Universität Augsburg, Universitätsstrasse 1, 86159 Augsburg, Germany

P. M. Petroff

Materials Department and Department of Electrical and Computer Engineering, University of California, Santa Barbara CA 93106, USA

petroff@engineering.ucsb.edu

Abstract:

This article reviews the fabrication, structural and optical properties of self-assembled In(Ga)As Quantum Post. We introduce the growth mechanism and present the resulting structural properties and electronic structure which provides a direct route to tunable intraband transitions. We show that in the interband spectrum, sharp optical transitions, single photon emission and tailored giant electrostatic dipole moments are observed. We demonstrate that these properties can be used for an exciton memory cell and a tunable Terahertz detector.

Outline:

A Introduction

B Structure, composition, physical and optical properties

1) Epitaxy of self-assembled quantum dots
2) Growth of self-assembled quantum posts.
3) Structure and chemical composition
4) Electronic structure: Single particle states form 8 band k.p calculations
5) Optical properties: Micro-photoluminescence of Single Quantum Posts
6) Excitons with giant electrostatic dipole moments

C Device applications:

1) Exciton memory cell
2) Terahertz absorption

D Future Directions
E Acknowledgements

A Introduction

The continuing trend of miniaturization in electronics and optoelectronics has been leading to nanoscale devices. Such structures not only allow for extremely high packing densities of integrated circuits but also approach a regime in which only a few electrons are responsible for device operations and functionality. Moreover, in such mesoscopic systems quantum effects play a dominant role for the device operation. The tailored density of states associated with the higher degree of confinement has led to devices with superior performances e.g. quantum dot lasers or single photons emitters [1-4]. In addition, these systems allow for the investigation of fundamental quantum effects in a semiconductor system. Quantum dot nanostructures became a key system since their 0-dimensional, atom-like density of states and electronic structure provide a unique property for the implementation of quantum logic schemes as well as a direct route to realize efficient semiconductor single photon emitters, a key device for quantum communication and quantum cryptography.

In particular, self-assembled quantum dots (QDs) realized in the In(Ga)As material system have attracted widespread interest due to their straight forward fabrication by molecular beam epitaxy (MBE) or metalorganic chemical vapor deposition (MOCVD) using a strain-driven self-assembly mechanism. This unique property allows not only for the fabrication of "artificial molecules" of coupled QDs but also for the more complex architectures like a QD crystals [5]. However, in all these approaches the size control remained rather limited and, therefore, the electron shell structure could not be engineered as freely as for quantum well superlattices. This major drawback for complex device applications like tunable Terahertz-devices or quantum cascade structures has to be overcome.

One very promising approach in this direction represents the quantum post (QP) a novel type of nanostructure. Its fabrication is based on the growth of self-assembled QDs, however, in contrast to this established system, the height of the QP can be controlled with nanometer precision. This unique feature adds the missing degree of freedom for engineering the electronic structure of 0-dimensional optically active nanostructures and could provide additional functionality through the incorporation of 2D and 3D confinement effects within the same nanostructure.

In this article we review the fabrication and chemical composition of QPs which are grown by MBE in the In(Ga)As/GaAs material systems. We continue by discussing the electronic structure which was calculated by an 8-band k.p method and showing their optical properties obtained by single QP photoluminescence spectroscopy. The tailored height of the QP gives rise to a characteristic shift of the emission in the presence of an external electric field. We will show that the Quantum Confined Stark Effect is in good agreement with the QP height which determines the magnitude of the maximum, giant electrostatic dipole moment of excitons. In the second part of the manuscript we will present two different device applications which directly take advantage of the tailored height and resulting electronic: A semiconductor exciton memory cell in a single QP, a device which uses the generation of long-lived spatially indirect excitons. Furthermore, we will present tunable intraband absorption of QPs for which the transition energy can

be adjusted both by a voltage but most importantly by the height of the QP over a large range of frequencies in Terahertz frequency range.

B Structure, composition, physical and optical properties of Quantum Posts

Self-assembled quantum dots (QDs) have been extensively studied for the last 15 years and much is known about their formation process in many III-V or II-VI semiconductors epitaxial thin films or epitaxial Si-SiGe films [5].

1) Epitaxy of self-assembled Quantum Dots

We briefly review some of the deposition and structural features for the InGaAs /GaAs QDs heterostructure system [6] which has been the most extensively studied. During the epitaxial deposition, the InGaAs thin film energy minimization takes place through the formation of InGaAs islands to relieve the built up elastic energy due to the InGaAs/GaAs lattice mismatch. The InGaAs islands formation minimizes the surface energy of the film and takes place only after the formation of a thin wetting layer (WL). The long-range diffusion of In over the GaAs surface towards a surface strain center (e.g. a surface step) allows the rapid formation and growth of a nucleation center for the island [7]. The island once covered with a layer of GaAs becomes an optically active quantum dot (QD). During the GaAs capping process, the island usually changes its shape and composition. The QD base usually has an elliptical shape with a shape anisotropy which is dependent on the growth temperature and In flux. The In surface diffusion on the (001) GaAs surface is more rapid along the [11-0]. The randomness of the nucleation and growth process leads to a composition and size distribution which usually strongly impacts the physical and device properties of the quantum dots. For the InGaAs/GaAs system, the QDs density can be controlled between $10^8 cm^{-2}$ to $10^{11} cm^{-2}$ by adjusting the deposition temperature between 480°C and 530°C. The QDs diameter and height range between 20-30 nm and 1.5 - 3 nm, respectively. The elastic strain distribution of the QDs is function of composition, size, surrounding matrix and deposition conditions. These effects strongly control the QDs physical properties and have been extensively studied using cross sectional STM [8] and TEM techniques [9] and QDs spectroscopy techniques.

2) Growth of self-assembled Quantum Posts

The InGaAs/GaAs quantum post (QP) is a self-assembled nanostructure [10] which relies on: a) the fast In diffusion on the GaAs (001) surface and b) surface exchange reactions which make the subsurface In atoms float to the surface and take the position of the Ga surface atoms. These exchange reactions which are driven by the bond formation energy between the group III and V atoms, have been well documented by STM cross section studied and are found in several III-V systems. The deposition for the QPs starts with the deposition of a seed QD and is followed by a repeated sequence of m GaAs monolayers (MLs) and n InAs MLs. The number m of MLs is large enough to cover the seed QD (Fig.1a) and n is ≈1 ML. For the GaAs {100}surface ≈7 ML of GaAs will be required to cover the 22nm thick seed QD. Following the deposition of the InAs ≈1ML

(Fig 1b), the group III fluxes are turned off for a time of 30 - 60 s, sufficient to observe the reappearance of the QD rebuilding of the RHEED pattern which changes from streaky to spotty chevron like pattern (Fig 1c-d). This deposition sequence is then repeated to form a QP with a height controlled by the number of sequences (Fig 1e). QPs with height up to 60 nm can be grown without the introduction of strain relieving dislocations.

3) Structure and chemical composition

Chemical analysis using Energy Dispersive X Ray (EDX) of the QPs and its surrounding QW matrix in a scanning transmission electron microscope (STEM), have shown that the QP consists of a short quantum wire terminated by a QD at each end. The QPs themselves are embedded in an lateral matrix with an In-content of 10%. Figure 1e) indicates the In content measured for the different areas in the QP and the lateral matrix (M). We note that this growth procedure is different from that used for stacking QDs in a position correlated fashion and where the QDs are separated by a thin (1-6 nm) GaAs layer [11].

The shape of the QP is usually conical with the top QDs having a larger size than the seed QD. Using $n = 1$ ML InAs in the deposition cycle will give a conical shape while reducing n below 1ML as the QP growth proceeds can give a cylindrical shape or an inverted cone shape QP [12].

4) Electronic structure: Single particle states from 8 band k.p calculations

One of the most important physical features of the QP can be seen in the analysis of the confined electrons and holes wave functions and energy levels. These are computed using an effective mass, 8-bands strain-dependent k.p model [10,13-15]. The detailed structural and composition information obtained from the STEM and EDX were used as input parameters for the calculation. As shown in Fig. 2 the single particle states for electrons or holes show a clear delocalization of the electron wave function for the z (along the growth direction) confined states while the holes remain localized in the top or bottom QDs. The QPs contain more than one z confined electron level and the intraband transitions between energy levels are in the technologically relevant Terahertz frequency region and can be adjusted by the height of the QP. This contrasts with conventional QDs where the intraband transition energies are in the 40-50meV range set by the x-y confinement and only one z confined state exists.

As will be seen later, the delocalized electrons and localized holes in the QPs allow for the possible switching of the heterostructure from a 2D confined to a 3 D confined regime under an applied electric field.

5) Optical Properties: Microphotoluminescence of Individual Quantum Posts

In Section B4 we presented theoretical calculations of the single particle electron and hole levels in QPs of different height. A standard characterization experiment for low-dimensional nanostructures is photoluminescence (PL) spectroscopy to assess the optical

quality of the investigated structure and to determine their electronic structure and few-particle interactions. Therefore, we performed micro-PL experiments on a series of individual QPs of 23 nm and 40 nm height. In these experiments the excitation laser was focused to a ~1 μm spot by a microscope objective which was also used to collect the QP emission. For spectral multi-channel analysis a grating monochromator equipped with lN$_2$ cooled CCD detector yielding a resolution < 0.5 meV was used. In Figure 3 we show typical low temperature (T=7K) PL spectra of individual 23 nm (a) and 40 nm (b) QPs where the excitation power is increased from P_0~1W/cm^2 for the bottom to 200P_0 for the top spectrum. Both QPs show qualitatively the characteristic shell-filling behavior also observed for conventional self-assembled QDs [16] as the excitation power and, therefore, the number of carriers captured into the nanostructure is increased. We find the emission of the QP ground state at 1280 meV and 1270 meV for the 23 nm and 40 nm QP, respectively. The first excited shell is typically found shifted 30-40 meV towards higher energy compared to the ground state. When directly comparing 23 nm and 40 nm QPs we find no characteristic fingerprints in the PL spectra due to strongly altered electronic structure resulting from the change of height. This finding might seem surprising in the first place, however it can be directly understood by considering the few-particle interactions in low dimensional nanostructures which are in the range of ~20 meV. These energy scales are dominating over the small single particle level spacing for high QPs leading to a QD-like PL signal for which interband electron-hole, exciton, recombinations are probed. An alternative explanation could be the strongly localized hole levels at the ends of the QP to which leads to an increased perturbation of the electron part of the exciton wavefunction.

Furthermore we analyzed the QP PL as a function of the sample temperature. In Fig 4 (a) we plot spectra recorded for an medium-density ensemble of 23 nm QPs over a range of temperatures from T = 5 K to 100 K. In the spectra three distinct peaks labeled 1, 2 and M can be identified which can be attributed to recombination in the QP, between QP-matrix and in the matrix, respectively [10]. As the temperature is increased peaks 2 and M show a clear quenching behavior whereas for peak 1 an increase of the signal is observed with a maximum at T = 40 K. Such a behavior is not typical for conventional QDs for which a continuous decrease of the PL signal is observed [17,18]. To gain further insight we extracted the integrated peak intensities and plot them in an Arrhenius representation in Fig. 4 (b). When examining the temperature dependence of the matrix peak (M) in more detail, two different slopes can be identified at low and high temperature which corresponds to energies of 2.5 meV and 38 meV, respectively. The same slope with opposite sign is also found for the increase of the QP groundstate peak (1) indicating that the same process is responsible for these effects [19]. One possible explanation is the thermal break-up of excitons in the matrix which results in an increased capture into the QPs giving rise to the observed increase of the signal. This explanation is further supported by temperature dependent spectroscopy of single QPs. A series of μ-PL spectra taken with low pump power is presented in Fig. 4 (c) over the same temperature range. For this QP we observe one dominant emission line (E = 1296 meV) at 10 K and a weaker feature shifted to higher energy by ΔE = 2.5 meV. All lines show a continuous shift to lower energy with increasing temperature due to a decrease of the bandgap. The high energy line gains intensity relative to the dominant feature at low temperatures up to 50 K close to the temperature at which we observe the maximum of the ensemble PL

intensity. Furthermore, the intensity of the higher energy peak quenches more rapidly as the temperature is raised further. Such behavior cannot be explained by thermal repopulation of a higher energy state like in a QD molecule [20] since no saturation is observed and equal intensities are observed for a temperature for which $k_BT = 4.3$ meV.

We further analyzed the PL emission of individual QPs. In Fig. 5 we show another spectrum of a 40 nm QPs recorded with higher spectral resolution and under pulsed optical excitation. For these particular QP three different emission lines are observed which can be assigned to the neutral ($X^0=1e+1h$), positively ($X^+=1e+2h$) and negatively charged ($X^-=2e+1h$) exciton. In particular the splitting between X^0 and X^- of 4.3 meV is typical for QD-like structures. To prove that this signal is indeed from an individual quantum emitter we performed an auto-correlation experiment on the X^0 emission (shaded gray in the main spectrum) to record the second-order correlation function $g^{(2)}(\tau)$ [21]. As shown in the inset of Fig. 5 we observe the expected pattern of peaks spaced by the repetition time of the laser. In this pattern the peak at $\tau = 0$ s is clearly suppressed characteristic for a single photon emitter. This finding demonstrates further the high optical quality of QPs comparable to conventional QDs. Taking into account also the increased carrier capture for elevated temperatures via the lateral matrix, QPs provide a large potential for applications as active emitters of single photon sources, lasers and other optoelectronic devices [1-4,22-25].

6) Excitons with giant electrostatic dipole moments

To further study the optical properties of QPs we embedded a single layer of these nanostructures at the center of a 220 nm wide intrinsic layer of a *n-i-p* junction. This type of device allows for (i) the application of a static electric field (*F*) oriented along the growth direction and, therefore parallel to the QP axis. (ii) Furthermore, electrical pumping of the QPs can be achieved by injection of electrons and holes from the doped layers.

When changing the gate voltage (V_B) on the device we can tune the axial electric field (*F*) which will give rise to a shift in the exciton emission line due to the Quantum Confined Stark Effect (QCSE) [26]. A typical example of *F*-dependent PL is shown in Figure 6 for a 23nm QP where the PL intensity is encoded in the gray-shade with dark regions indicating high PL intensity. The tilting of the bands is also shown schematically to illustrate the change of *F* when V_B is tuned. In the spectra observe a series of emission lines which show a characteristic shift due to the QCSE. One typical line is highlighted by the dashed line which shows initially a relatively weak Stark-shift which increases and asymptotically adopts a strong and linear behavior. Such shifts have been previously reported for coupled QD systems where the exciton groundstate undergoes a field-driven transition from a spatially direct exciton (*e* and *h* in the same dot) to a spatially indirect exciton (*e* and *h* in different dots) [27]. A similar effect also occurs in QPs where *e* and *h* are separated by the electric field due to their opposite charge and pulled towards opposite ends of the post. As this separation proceeds the electrostatic dipole moment is

increasing from a QD-like small value at low F (high V_B) where e and h are bound to a large value at high F (low V_B) where e and h are dissociated and localized at opposite ends. This process and the resulting dipole moments are shown schematically in Fig. 6. Since the magnitude of the QCSE is proportional to the dipole moment $\Delta E_{Stark} = p \cdot \Delta F$ the shift rate increasing accordingly as the exciton undergoes the described field-driven transition from direct to indirect character. In the limit of high electric fields the e-h separation d_{eh} asymptotically approaches the height of the QP h_{QP} and remains constant as the centers of gravity of the two wavefunctions are localized close to the opposite ends of the QP. Therefore, the resulting dipole moment reaches a maximum $p_{\max} = e \cdot d_{eh} = e \cdot h_{QP}$ giving rise to strong linear Stark shift. Over the full range of electric field we therefore expect a weak shift for low F where Coulomb attraction dominates and the dipole moment is small which increases as the Stark contribution is increasing and dissociates the exciton towards opposite ends of the QP giving rise to the observed asymptotical linear shift at higher F. To confirm this assumption we analyzed the emission line marked in Fig. 6 and plotted its energy as a function of F as symbols in Fig. 7. The PL energy is well reproduced by a linear fit (line) in the regime of high electric fields. Furthermore, the dipole moment obtained: $p_{\max} = e \cdot (20.2 \pm 0.2)$ nm is in excellent agreement with the nominal value for h_{QP}=23 nm.

A closer examination of the spectra shown in Fig. 6 reveals that the intensity strongly decreases as the transition adopt more indirect character. This finding is also expected since the e and h wavefunctions are pulled apart and, therefore their overlap decreases. This directly leads to a reduction of the exciton oscillator strength and increase in the radiative lifetime giving rise to the suppression of the radiative emission. This phenomenon can be directly used to store individual excitons in a single nanostructure which we demonstrate in Section C1. For a 40nm QP, the observed dipole moment is more than 10 times larger than for a QD.

In addition to the discussed wide range energy tuning of excitonic transitions using the QCSE our device allows also for electrical pumping of the QPs which is shown schematically in Fig. 8 (a). Under forward bias e and h are injected from the respective contacts into the QPs where they radiatively recombine. This injection becomes dominant as V_B is tuned above the flatband voltage. Its calculated value of 1.43 V is marked in the current-voltage trace of our device shown in Fig. 8 (b). For V_B>1.43 V we observe the onset of the electroluminescence (EL) signal which is shown in Fig. 8 (c). The signal increases as the forward bias and current increase and, therefore, the electrical injection becomes stronger. We want to note, that the EL lines marked by the box in Fig. 8 (c) correspond to the QPs studied by F-dependent PL shown previously. This demonstrates that QPs are suitable for both electrically and optically pumped applications in opto- and quantum-electronic devices.

C Device application

1) Exciton memory cell

The unique QCSE of QPs allows for the realization of a scheme for storing an indirect exciton in a single nanostructure [28]. Our method which is shown schematically in Fig. 9 uses a sequence of three electrical pulses for gating: the sample bias voltage, the laser to write excitons, and the detector to read the stored signal. For each step the spatial distribution of the electron and hole and the band structure are depicted schematically. The storage sequence starts with a reset step under a large reverse bias ($V_{reset} \sim$ -5 V) under which carriers can tunnel out of the QP. In the next step, the sample bias is raised to V_{store}, a level where the exciton is in a spatially indirect long-lived state whilst tunneling out of the QP remains suppressed. At the start of this storage interval, the laser is turned on for 500 ns to write electron hole pairs into the QPs by photogeneration. During storage both carriers are localized *in the same* nanostructure but remain spatially separated due to the applied field. When the sample bias is brought back close to flat-band (V_{read}) for a time t_{read} = 1 μs, the stored excitons become spatially direct. Under these conditions the electron and hole wavefunctions overlap and radiative recombination can occur. The emitted photons are then detected during this read step. To reduce the dark count level the detector is read out only while the read voltage is applied. Thus, we define the storage time (t_{store}) as the difference between the time when the "write" laser is turned off and the time a "read" voltage is applied.

To demonstrate this scheme we used a sample with a low surface density of QPs ($\sim$1000/μm^2). The store and read voltages were set to V_{store} = +0.5 V and V_{read} = +1.5 V, respectively. Typical storage spectra as a function of wavelength are shown in Fig. 10 for t_{store} = 20 μs and 220 μs. We find a pronounced peak centered at λ = 987 nm with a width of 34 nm consistent with the QP ground state PL for a QP ensemble. The intensity of this storage peak does not decrease when the storage time is increased by more than one order of magnitude. Thus finding clearly demonstrates persistent and loss-free storage of excitons in a single nanostructure.

Two control experiments were performed to demonstrate that we are indeed storing an spatially indirect exciton. In the first one, the read voltage is set to a level at which the exciton ground state remains indirect. For this condition, we do not expect to detect a stored signal since radiative recombination strongly suppressed for indirect excitons. To confirm that the read signal originates from excitons photogenerated by the write laser and not from carriers electrically injected from the *p*- and *n*-doped layers, a second control experiment was done in which the laser remains off. No storage signal should be detected even though the read voltage is applied since no excitons were written. The results of these two control experiments are shown as blue (no read) and green (no write) symbols for t_{store} = 20 μs in Fig. 10. Clearly, no signal is detected in both cases demonstrating that we store excitons in the QPs, which are later read-out simply by changing the gate potential on our device.

The exciton storage could be demonstrated with a single quantum post. The maximum storage signal without any contributions from electroluminescence was obtained for a read voltage of $\sim$ +1.5 V. We observed as pronounced increase of the storage signal when V_{read} was increased from +1 V to +1.5 V. This data is shown in Fig. 11 and clearly

demonstrates that with increasing forward bias (reducing F) for a higher fraction of QPs the *e-h* wavefunction overlap is restored and reconversion into the photonic domain occurs for a larger QPs population. Furthermore, carriers can be injected electrically in the QPs using our device from the *p-* and *n*-contacts. This allows operating our exciton memory purely electrically by replacing the optical pump by a high forward bias electrical pulse. After fast electrical switching to the storage voltage, cascaded emission will occur after which spatially indirect excitons remain in the QPs. For these radiative recombination is suppressed and these excitons are stored. A comparison of optically and electrically pumped storage spectra is shown in Fig. 12 for a +3.5V injection pulse demonstrating the possibility of an electrically driven exciton memory. The broadening towards shorter wavelength could arise due to preferential formation of charged excitons since the QPs are embedded in the center of the *i*-region in our device. In the limit of a single QP, this purely electrical operation could be used e.g. for electrically triggered single photon generation.

In Fig. 13 we plot the integrated storage signal as a function of $t_{storage}$ for three different values of $V_{storage}$. For $V_{storage}$ = +0.1 V ($F \sim$ 50 kV/cm) we observe a slow exponential decay of the storage signal with a time constant of 30±7 ms. As $V_{storage}$ is lowered and the electric field is increasing we observe faster decays with 7±1 ms and 0.7±0.2 ms for 0.0V ($F \sim$ 54 kV/cm) and -0.1V ($F \sim$ 58 kV/cm), respectively. For the radiative lifetime we expect the opposite voltage dependence since the increasing separation of electron and hole reduces their wavefunction overlap. This is confirmed by calculations of the radiative lifetime of spatially indirect excitons as a function of F for a realistic QP morphology using a strain-dependent 8-band k.p model shown by the black line in Fig 14. In contrast, the observed lifetime shortening is well explained by a reduction of the tunnelling time between the confined QP states and the GaAs matrix schematically shown in Fig. 13. In a simple model the tunneling time ($t_{tunnelling}$) can be described by a 1-dimensional *WKB* approximation (Fowler-Nordheim tunnelling) given by

$$\frac{1}{t_{tunnelling}} = \frac{\hbar\pi}{2m_e^* L^2} \cdot \exp\left[\frac{-4}{3\hbar eF}\sqrt{2m_e^* E_{ion}^3}\right], (1).$$

Here, m_e^*, L and E_{ion} are the electron effective mass, the length of the confinement potential and the ionization energy, respectively. We assume that electron tunneling is faster than that of holes due to their smaller effective mass [29] and compare $t_{tunnelling}$ (red line) with the experimentally measured decay times in Figs. 13 and 14. The experimental data is well reproduced using this model with m_e^* = 0.062 m_0 and E_{ion} = 170 meV which are in good agreement with the PL data and our *k·p* calculations. At $F \sim$ 50 kV/cm the timescales for tunneling (black) and radiative (red) losses are in the range giving rise to the maximum storage times of $\sim$ 50 ms. Since our experimental data is reproduced by the computed behavior for tunnel escape of electrons, we identify this process as the dominant loss mechanism in this field range. Clearly, the storage time could be further increased to seconds, limited only by radiative losses by suppressing tunneling using e.g. the higher bandgap of AlGaAs for capping the QPs. However, these timescales are

sufficiently long to study spin effects [30,31] even under non-resonant pumping of the QPs [32].

Finally, we investigated the temporal statistics of the storage signal by performing a time-correlated single photon counting experiment of the storage signal. In Fig. 15 (a) and (b) the logarithmic number of detection events is plotted as a function of the delay Δt between the time the read voltage is turned on and the time the reconverted photon is detected. For the storage signal we find a narrow peak with a width of 15 ns and rise and fall times of t_{rise} = 3.5 ns and t_{fall} = 5.0 ns, respectively. No more photons are detected afterwards over the duration (t_{read} = 1 µs) of the read voltage pulse as shown in the Fig. 15 (a). We want to note that this fast read-out excludes injection of electrons and/or holes from the doped reservoirs which are separated from the QPs by 110 nm intrinsic GaAs barriers and further confirms storage of both electrons and holes within the QPs. Moreover, from modeling the electrical properties of our diode we find that this fast read-out is indeed limited only by the *RC* time constant. This can be optimized further for efficient, fast exciton-photon conversion for quantum information implementations or triggered single photon generation.

2) Probing the QPs intrasubband energy levels using THz absorption spectroscopy

The computed energy level structure computed for two QPs with different height shown in Figure 2 indicates that the QPs structure could find used for THz device applications. Here we present briefly the results of experiments, which probe the intrasubband energy levels in QPs with different dimensions. The technique used for probing the QPs energy levels is similar to that previously used for QDs [33]. It combines capacitance spectroscopy with FTIR absorption spectroscopy. The QPs device structure shown in Figure 16 allows for the loading of a QP lowest energy level via tunneling from a back gate electron reservoir. The loading for a large ensemble of QPs ($\approx 10^8$) with a height of 30nm is followed using capacitance-voltage (C-V) measurements and is detected by the shoulder in the C-V curve at the lowest voltage [34]. By measuring the C-V of a similar device structure containing only a 30 nm In$_{.1}$Ga$_{.9}$As quantum well (QW) matrix, the second capacitance plateau at -1V in Figure 16 is found to correspond to the electron loading of the QW ground state.

The absorption measurements are carried out for the same samples using an FTIR Michelson interferometer as the THz source and a side illumination and detection [8]. Low temperature (T = 5 K) absorption measurements on a device containing the QPs and the In$_{.1}$Ga$_{.9}$ As matrix quantum well are shown in Figure 17 along with that of a sample containing only the In$_{.1}$Ga$_{.9}$ As quantum well. The spectra are obtained with an applied voltage bias which ensures loading of both the quantum posts and surrounding quantum well matrix. The shaded area in Figure 17(B) is obtained by deconvolution of the absorption spectrum in Figure 17(A) from that in (B) and corresponds to the QPs absorption spectrum. The origin of the QPs absorption line broadening can probably be attributed to the lateral size and composition fluctuations in the QPs ensemble. The

10

applied field required to load electrons in the QPs will also result in a QCSE which will vary with QPs sizes and composition and may also contribute the broadening of the QPs absorption line. We also note the stronger absorption of the QPs layer which compared to the QW sample occupies a few percent of the sample volume.

D Future directions

In this article we reviewed the fabrication, structure and chemical composition of self-assembled QPs along with their calculated electronic structure. We demonstrated that QPs exhibit excellent optical properties manifesting in sharp PL line width and single photon emission. We showed that the tailored height of the QPs can be used to generate giant static excitonic dipole moments that are producing characteristic linear QCSE and ultra-long radiative lifetimes. In the last part of the article we showed two direct applications: an exciton memory cell based on a single nanostructure and a tunable Terahertz detector. These two devices are exemplary for the wide range of applications of QPs from optical amplifiers, lasers, single photon emitters and phase modulators as well as detectors and photovoltaics [1-4, 22-25]. In addition, the high structural, optical quality and discrete energy spectrum and the possibility of direct integration in optical microcavities [4,22,35] can be also used for the implementation of quantum logic based on excitons [36-38] or spins [39-42] or cavity-QED experiments [35]. Moreover, QPs could also allow for combined optical and electrical transport spectroscopy of the same single one-dimensional semiconductor nanostructure due to its controllable height and optical and electrical access. Besides few exemptions [43] either the transport [44] or the optical properties [45] can be probed for the same embedded quantum wire. In particular in the case of quantum wires defined in high-mobility 2-dimensional electron systems at single heterointerfaces no confinement for hole exists and, therefore, optical investigations are not possible [46].

References:

[1] D. Bimberg, J. Phys. D: Appl. Phys. 38 (2005) 2055-2058.

[2] D. J. Mowbray, M. S. Skolnick, J. Phys. D: Appl. Phys. 38 (2005) 2059–2076.

[3] P. Bhattacharya, S. Ghosh, A. D. Stiff-Roberts, Annu. Rev. Mater. Res. 34 (2004) 1.

[4] A. J. Shields, Nature Photonics 1 (2007) 215-223.

[5] J. Stangl, V. Holý, G. Bauer, Rev. Mod. Phys. 76 (2004) 725-783.

[6] D. Leonard, M. Krishnamurthy, C. M. Reaves, S. P. DenBaars, and P. M. Petroff, Appl. Phys. Lett 63 (1993), 3203.

[7] B. D. Gerardot, G. Subramanian, S. Minvielle, H. Lee, J. A. Johnson, W. V. Schoenfeld, D. Pine, J. S. Speck, P. M. Petroff, J. of Crystal Growth, 236 (2002) 647-654.

[8] W. Wu, J. R. Tucker, G. S. Solomon, and J. S. Harris, Appl. Phys. Lett. 71 (1997) 1083.

[9] P. B. Joyce, T. J. Krzyzewski , G. R. Bell. B. A. A. Joyce, T. S. Jones, Phys. Rev. B 58 (1998) R15981.

[10] J. He, H. J. Krenner, C. Pryor, J. P. Zhang, Y. Wu, D. G. Allen, C. M. Morris, M. S. Sherwin, P. M. Petroff, Nano Lett. 7 (2007) 802-806.

[11] T. Kita, N. Tamura, O. Wada, M. Sugawara, Y. Nakata, H. Ebe, Y. Arakawa, Appl. Phys. Lett. 88 (2006) 211106.

[12] L. H. Li, P. Ridah, G. Patriarche, N. Chauvin, A. Fiore, Appl. Phys. Lett. 92 (2008) 121102.

[13] C. Pryor, Phys. Rev B 57 (1998) 7190.

[14] I. Vurgaftman, I. R. Meyer, L. R. Ram-Mohan, J. Appl. Phys. 89 (2001) 5815.

[15] H. J. Krenner, C. Pryor, J. He, J.P. Zhang, Y. Wu, C.M. Morris, M.S. Sherwin, and P.M. Petroff, Physica E 40 (2008) 1785-1789.

[16] S. Raymond, S. Fafard, P. J. Poole, A. Wojs, P. Hawrylak, S. Charbonneau, D. Leonard, R. Leon, P. M. Petroff, J. L. Merz, Phys. Rev. B 54 (1996) 11548-11554.

[17] J. C. Kim, H. Rho, L. M. Smith, H. E. Jackson, S. Lee, M. Dobrowolska, and J. K. Furdyna, Appl. Phys. Lett. 75 (1999) 214.

[18] M. Bayer, A. Forchel, Phys. Rev B 65 (2000) 041308.

[19] W. H. Jiang, X. L. Ye, B. Xu, H. Z. Xu, D. Ding, J. B. Liang, and Z. G. Wang, J. Appl. Phys. 88 (2000) 2529.

[20] T. Nakaoka, E. C. Clark, H. J. Krenner, M. Sabathil, M. Bichler, Y. Arakawa, G. Abstreiter, J. J. Finley, Phys. Rev. B 74 (2006) 121305.

[21] P. Michler, A. Kiraz, C. Becher, W.V. Schoenfeld, P. M. Petroff, L. Zhang, E. Hu, A. Imamoglu, Science 290 (2000), 2282-2285.

[22] S. Strauf, N. G. Stoltz, M. T. Rakher, L. A. Coldren, P. M. Petroff, D. Bouwmeester, Nature Photonics 1 (2007) 704-708.

[23] T. Akiyama, H. Kuwatsuka, T. Simoyama, Y. Nakata, K. Mukai, M. Sugawara, and O. Wada, IEEE J. Quantum Electron 37 (2001) 1059.

[24] G. Moreau, A. Martinez, D. Y. Cong, K. Merghem, A. Miard, A. Lemaître, P. Voisin, P. Ramdane I. Krestnikov, A. R. Kovsh, M. Fischer, J. Koeth, Appl Phys. Lett. 91 (2007) 091118.

[25] I. B. Akca, A. Dana, A. Aydinli, M. Rossetti, L. Li, A. Fiore, N. Dagli, Opt. Express 16 (2008) 3439-3444.

[26] P. W. Fry, I. E. Itskevich, D. J. Mowbray, M. S. Skolnick, J. J. Finley, J. A. Barker, E. P. O'Reilly, L. R. Wilson, I. A. Larkin, P. A. Maksym, M. Hopkinson, M. Al-Khafaji, J. P. R. David, A. G. Cullis, G. Hill, J. C. Clark, Phys. Rev. Lett. 84 (2000) 733-736.

[27] H. J. Krenner, M. Sabathil, E. C. Clark, A. Kress, D. Schuh, M. Bichler, G. Abstreiter, J. J. Finley, Phys. Rev. Lett. 94 (2005) 057402.

[28] H. J. Krenner, C. E. Pryor, J. He, and P. M. Petroff, Nano Lett. 8 (2008) 1750–1755.

[29] P. W. Fry, J. J. Finley, L. R. Wilson, A. Lemaitre, D. J. Mowbray, M. S. Skolnick, M. Hopkinson, G. Hill, J. C. Clark, Appl. Phys. Lett. 77 (2000) 4344-4346.

[30] M. Kroutvar, Y. Ducommun, D. Heiss, D. Schuh, M. Bichler, G. Abstreiter, J. J. Finley, Nature 432 (2004) 81-84.

[31] A. Greilich, D. R. Yakovlev, A. Shabaev, Al. L. Efros, I. A. Yugova, R. Oulton, V. Stavarache, D. Reuter, A. Wieck, M. Bayer, Science 313 (2006) 341-345.

[32] S. Trumm, M. Wesseli, H. J. Krenner, D. Schuh, M. Bichler, J. J. Finley, M. Betz, Appl. Phys. Lett. 87 (2005) 153113.

[33] H. Drexler, D. Leonard, W. Hansen, J. P. Kotthaus, P. M. Petroff, Physical Review Letters 73 (1994) 2252.

[34] C. Morris, D. Stehr, H. Kim, T. A. Truong, H. J. Krenner, P. M. Petroff, M. S. Sherwin (in preparation).

[35] A. Badolato, K. Hennessy, M. Atatüre, J. Dreiser, E. Hu, P. M. Petroff, A. Imamoglu, Science 308 (2005) 1158-1116.

[36] E. Biolatti, R. C. Iotti, P. Zanardi, F. Rossi, Phys. Rev. Lett. 85 (2000) 5647-5650.

[37] H. J. Krenner, S. Stufler, M. Sabathil, E. C. Clark, P. Ester, M. Bichler, G. Abstreiter, J. J. Finley, A. Zrenner, New J. Phys. 7 (2005) 184.

[38] S. Stufler, P. Ester, A. Zrenner, M. Bichler, Phys. Rev. Lett. 96 (2006) 037402.

[39] V. Cerletti, W. A. Coish, O. Gywat, D. Loss, Nanotechnology 16 (2005) R27-R49.

[40] H. J. Krenner, E. C. Clark, T. Nakaoka, M. Bichler, C. Scheurer, G. Abstreiter, J. J. Finley, Phys. Rev. Lett. 97 (2006) 076403.

[41] M. Scheibner, M. F. Doty, I. V. Ponomarev, A. S. Bracker, E. A. Stinaff, V. L. Korenev, T. L. Reinecke, D. Gammon, Phys. Rev. B 75 (2007) 245318.

[42] D. Kim, S. E. Economou, S. C. Bădescu, M. Scheibner, A. S. Bracker, M. Bashkansky, T. L. Reinecke, D. Gammon, Phys. Rev. Lett. 101 (2008) 236804.

[43] S. F. Roth, H. J. Krenner, D. Schuh, M. Bichler, M. Grayson, Appl. Phys. Lett. 89 (2006) 032102.

[44] A. Yacoby, H. L. Stormer, N. S. Wingreen, L. N. Pfeiffer, K. W. Baldwin, K. W. West, Phys. Rev. Lett. 77 (1996) 4612.

[45] A. R. Goni, L. N. Pfeiffer, K. W. West, A. Pinczuk, H. U. Baranger, H. L. Stormer, Appl. Phys. Lett. 61 (1992) 1956.

[46] B. E. Kane, G. R. Facer, A. S. Dzurak, N. E. Lumpkin, R. G. Clark, L. N. Pfeiffer, K. W. West, Appl. Phys. Lett. 72 (1998) 3506.

Figures:
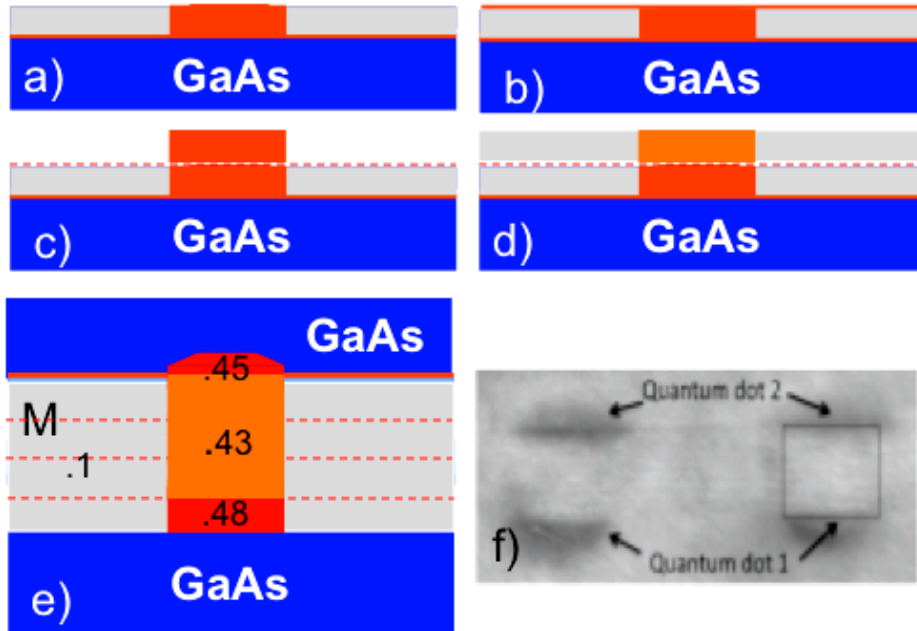
Figure 1 - a-c) Schematic of the deposition sequence on top of the seed QD. The grey shades area indicate the 7ML of GaAs deposited to cover the seed QD. The solid and dashed red line indicate the ML of InAs before and after the rebuilding of the QD on top of the seed QD.. The numbers in 1e) indicate the measured In content. The dashed red line is left to suggest that the 10% In remaining in the QW matrix M may be mixed by surface exchange reactions with 1-3ML of GaAs. 1 f) Cross section STEM showing the contrast associated with the top and bottom QDs at each end of 23 nm tall QPs. The dash lines outlines the QP shape [10].
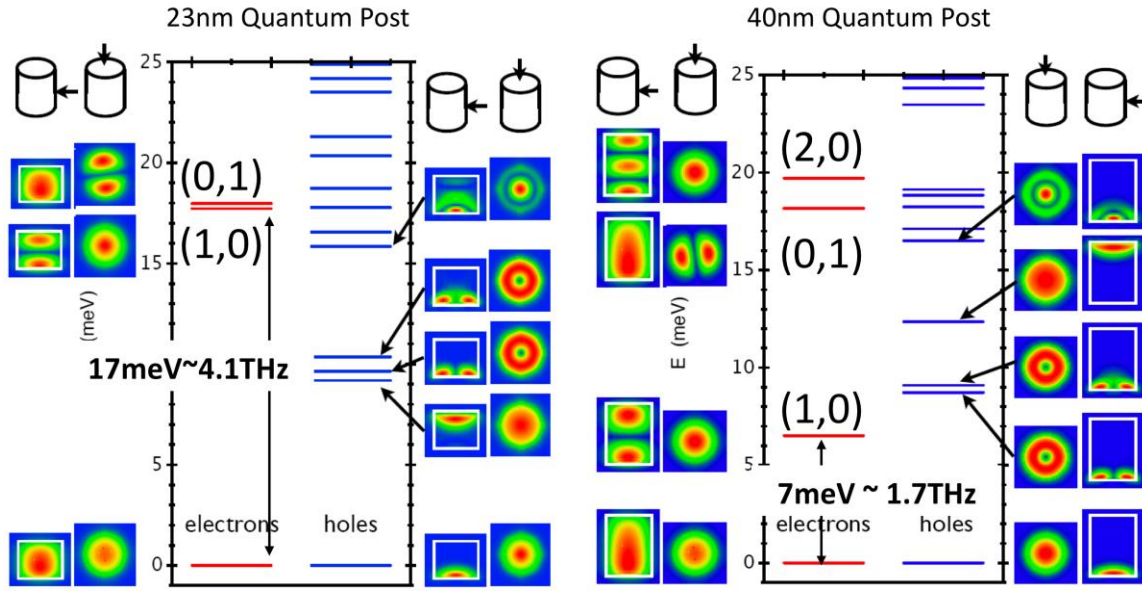
Figure 2 - Computed wave functions probability densities and electrons and holes energy levels for a 23nm and a 40nm QP for the 2 directions indicated in the figure. The level energy scales are referenced to the z (0,0) confined ground state. In addition to the ground state, the 23nm QP contains 1 additional electron (1,0) z confined level and the 40nm QP contains 2 additional electrons (1,0) and (2,0) z confined levels. As indicated by the probability density mapping, the electron wave function is delocalized for these levels. All other levels correspond to laterally confined states. The hole wave functions are localized at the top or bottom quantum dots [10,15].
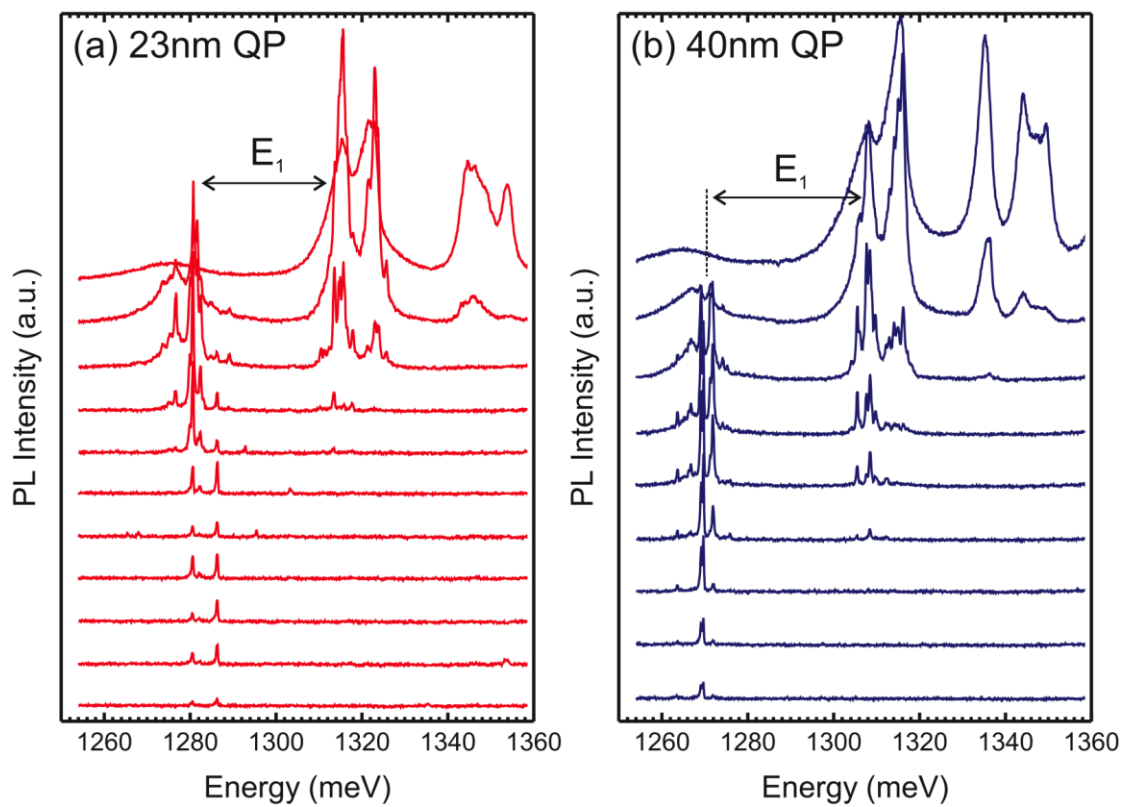
Figure 3 – Power dependent μ-PL spectral of individual 23 nm (a) and 40 nm (b) QPs.
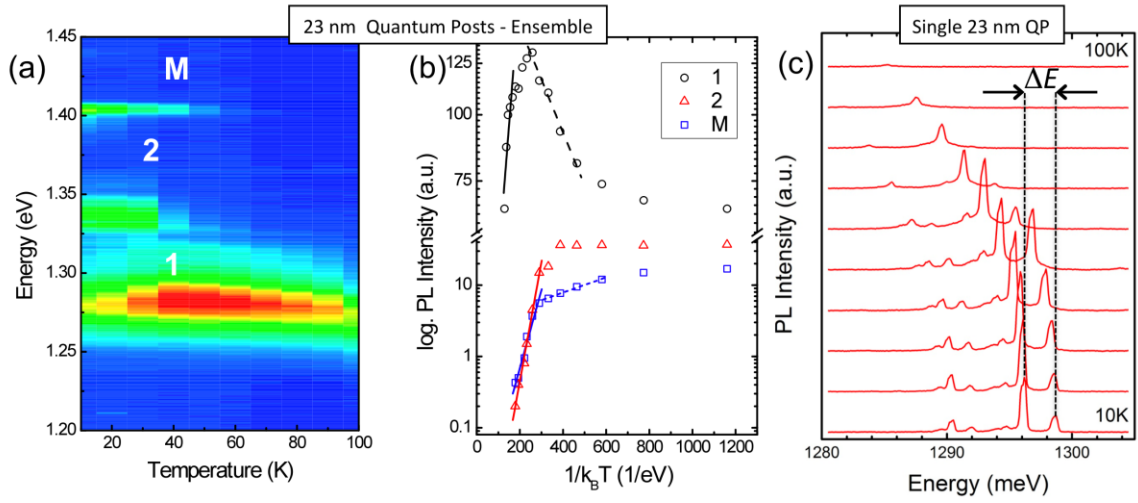
Figure 4 – Temperature dependent PL spectroscopy of 23 nm QPs. (a) Ensemble PL in false color representation. (b) Extracted peak intensities (symbols), Arrhenius fits (lines) and obtained activation energies. (c) Single QP spectra as a function of temperature.

18
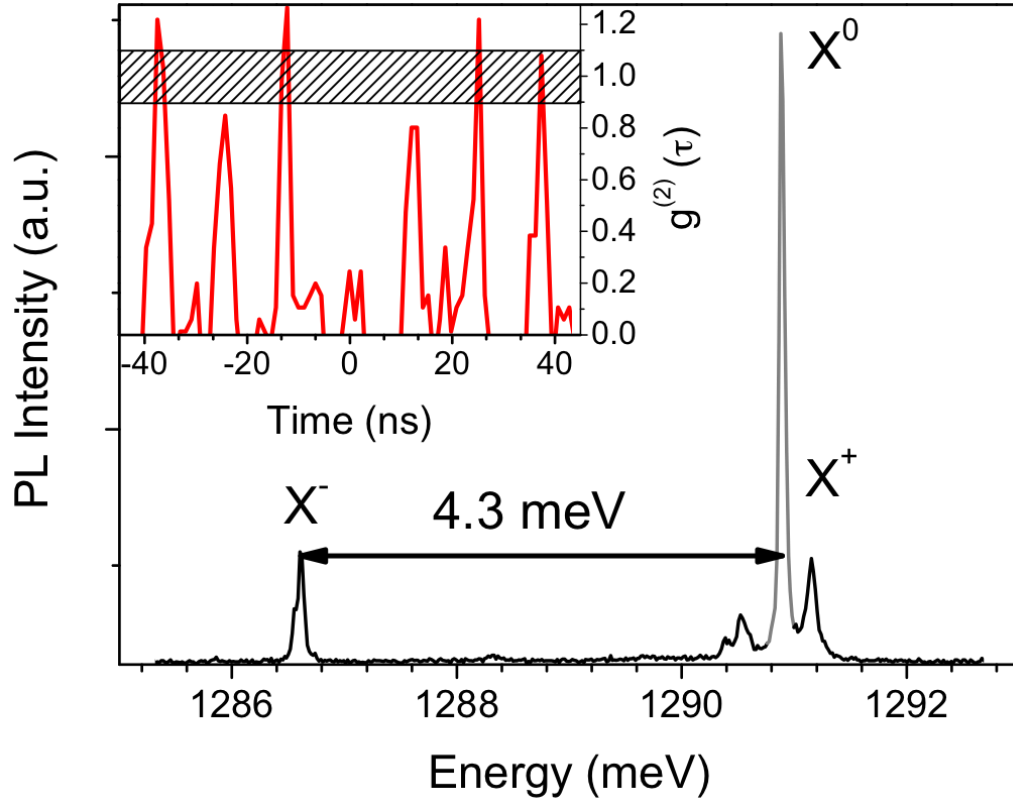
Figure 5 – A single 40 nm QP: μ-PL spectrum (main panel) and second order correlation function (inset) measure for the X^0 line (gray shaded) proving single photon emission.
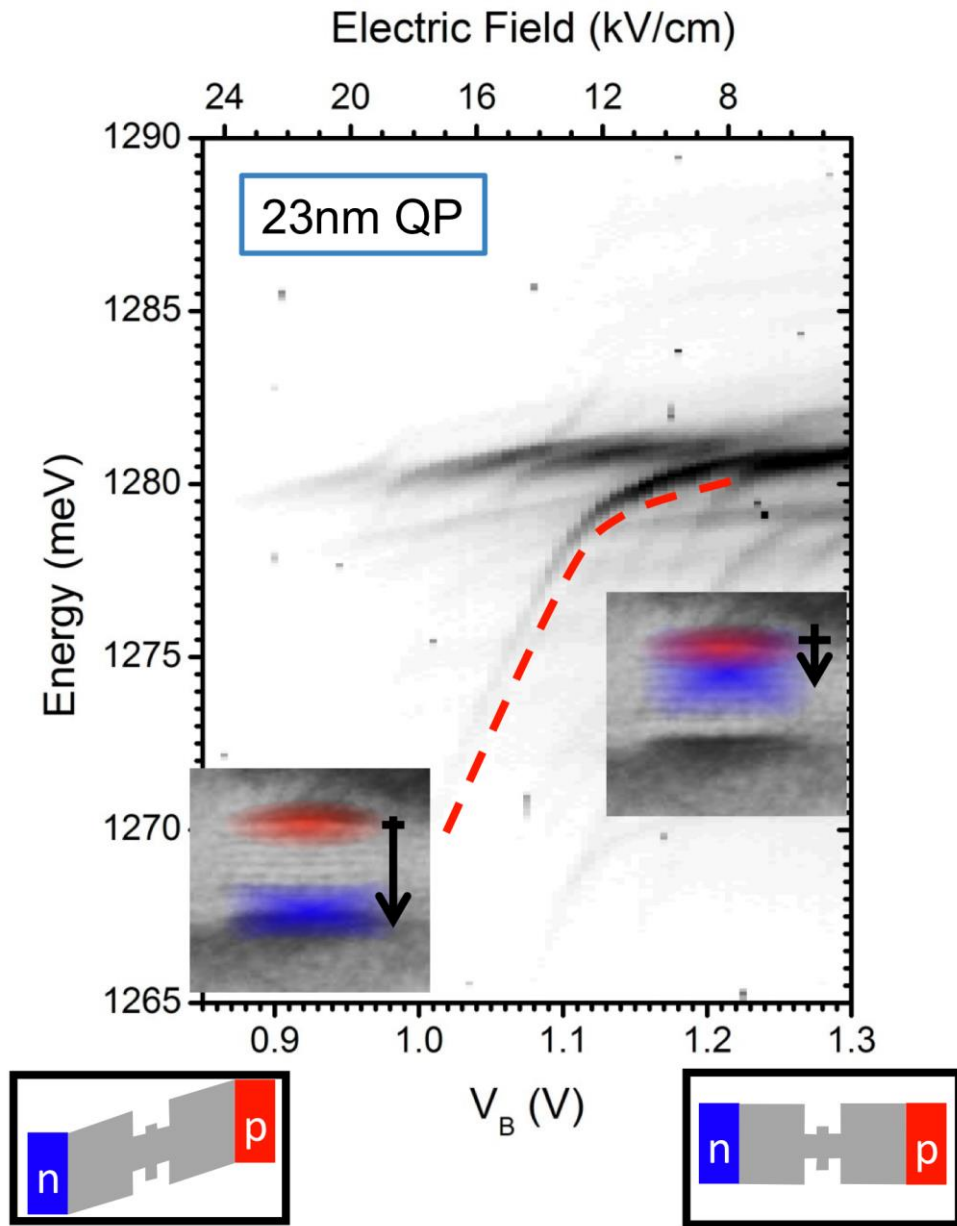
Figure 6 – Electric field dependent PL of a single 23 nm QP. The tilt of the bandstructure and the spatially direct and indirect exciton configurations are shown schematically.
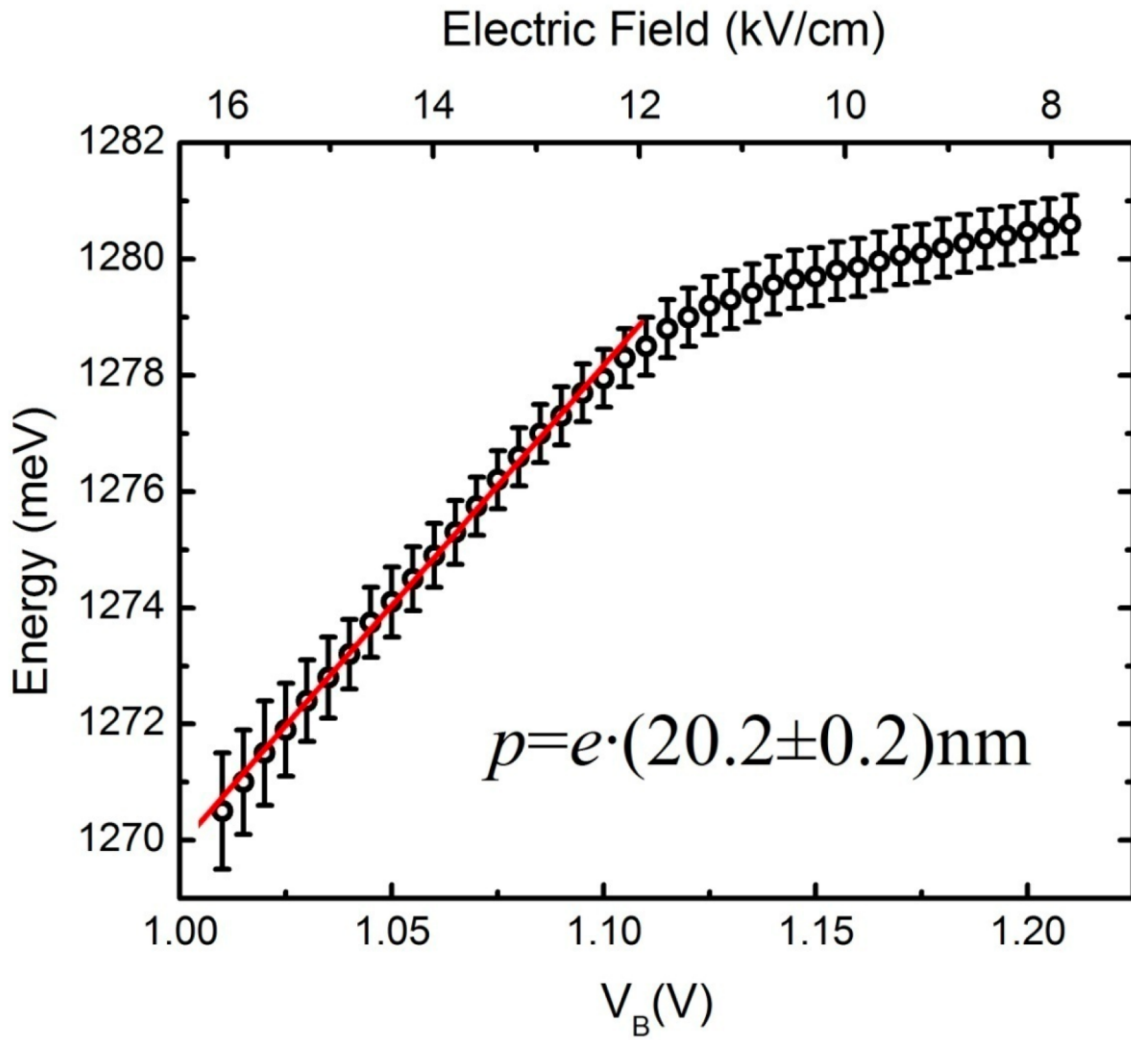
Figure 7 – Extracted PL energies (symbols) as function of the applied electric field and linear fit in the high *F*-regime (line).
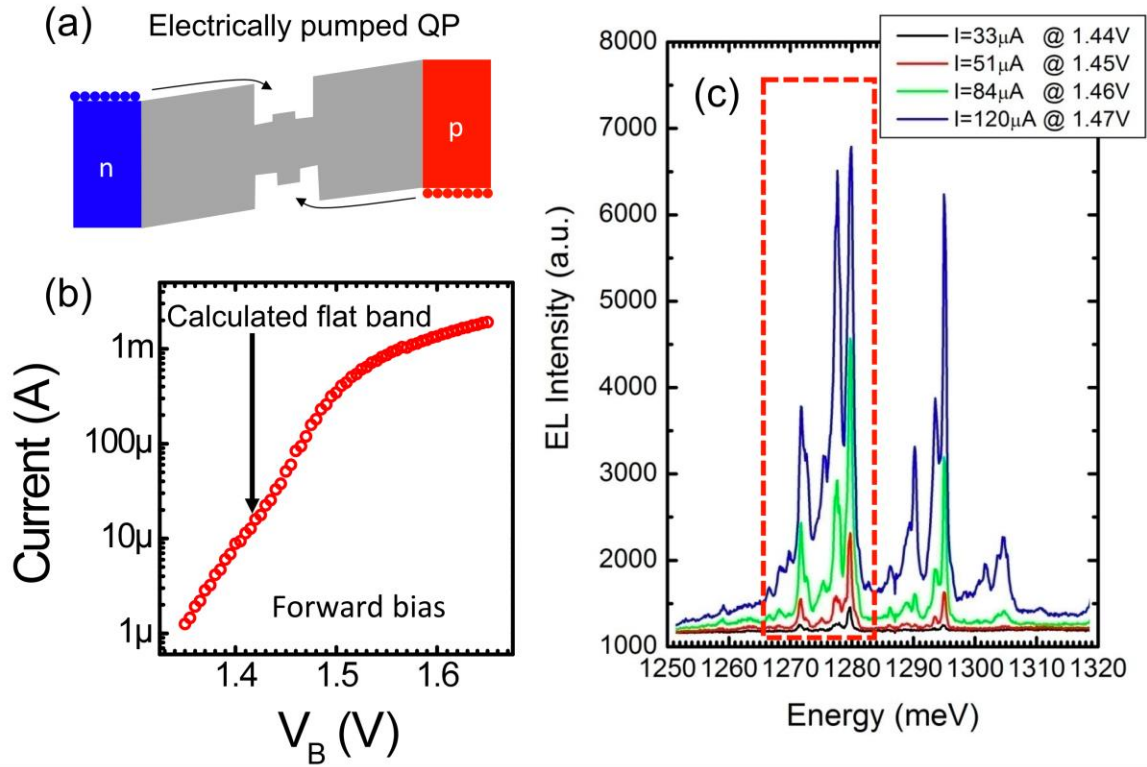
Figure 8 – Electroluminescence of QPs. (a) Schematic of electrical pumping of QPs. (b) Current-voltage trace under forward bias with calculated flat band voltage marked. (c) Electroluminescence spectra as a function of the forward voltage and current of individual QPs. The box marks EL-emission of the same QP of which PL spectra are shown in Fig. 6
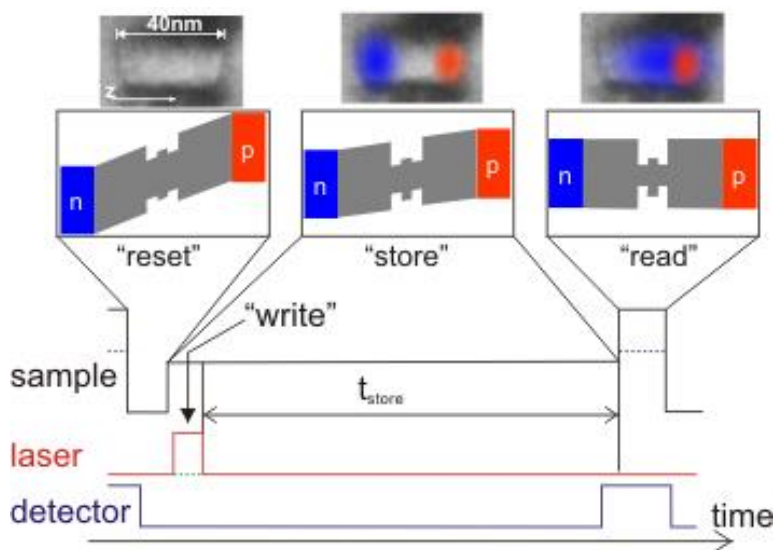
Figure 9- Electrical gating scheme for storing excitons in Quantum Posts.
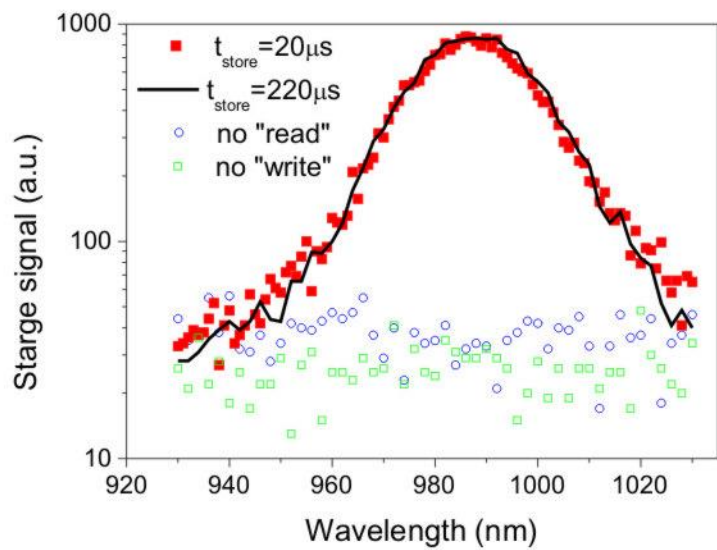
Figure 10 – Storage spectra for different storage times with reference traces of the control experiments.
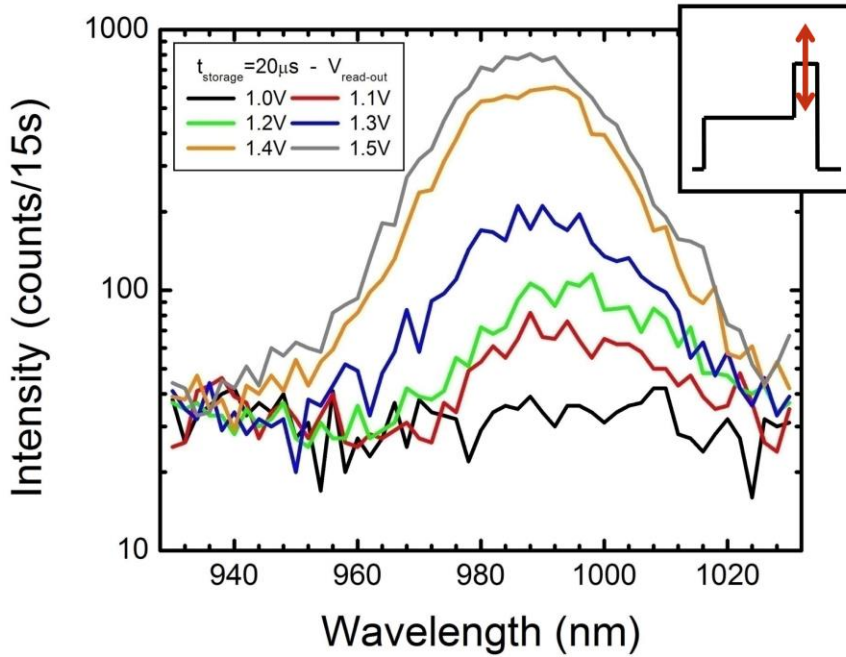
Figure 11 – Storage spectra as a function of the read-out voltage pulse amplitude as shown schematically in the inset.
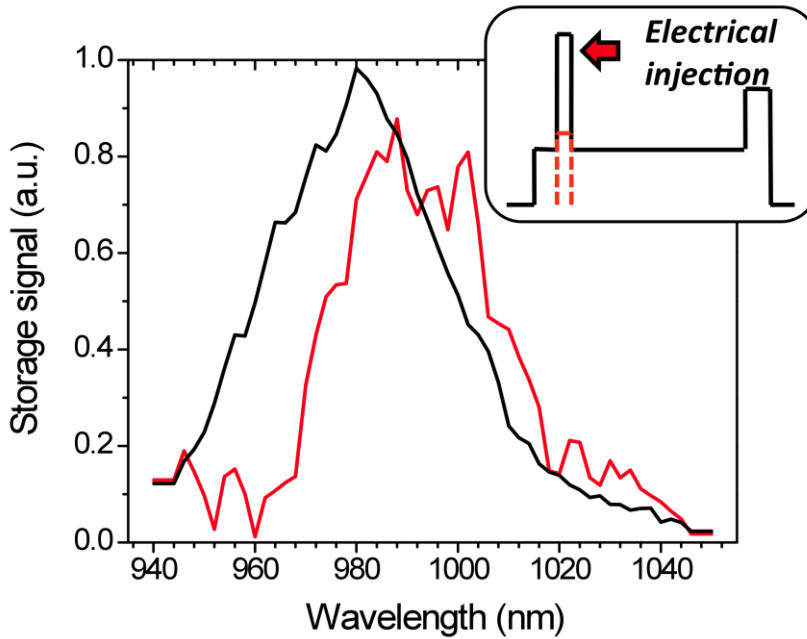
Figure 12 – Storage spectra under optical (red) and electrical (black) injection. Under electrical injection the laser write pulse is replaced by an forward bias voltage pulse, shown in red and black schematically in the inset.
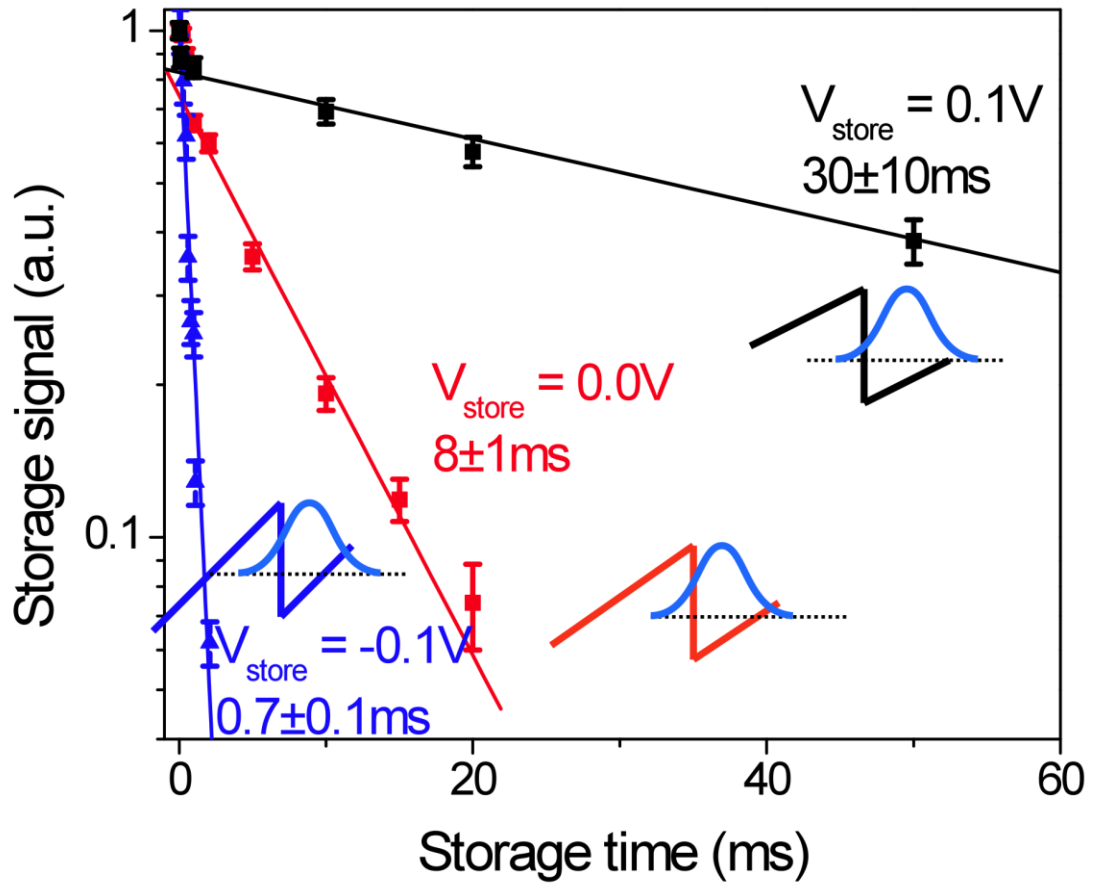
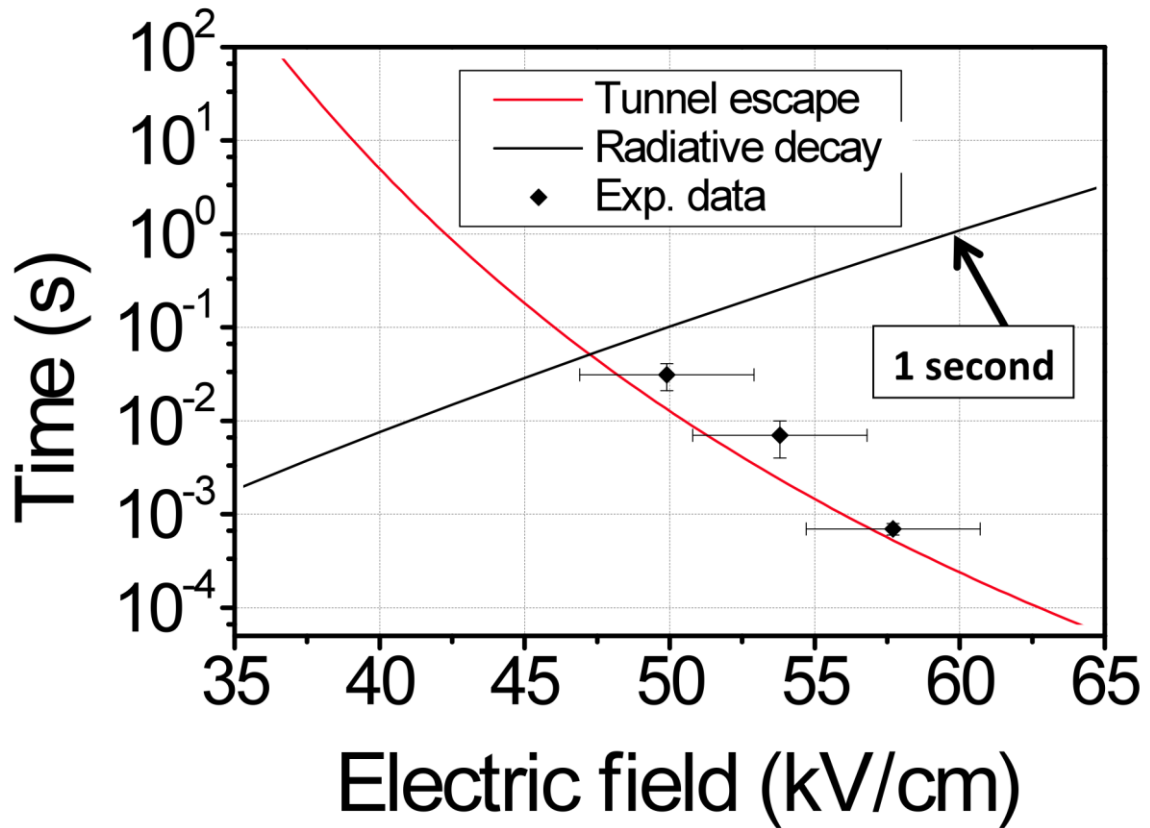Figure 13 – Time transients of the storage signal for different values of V_{store}.
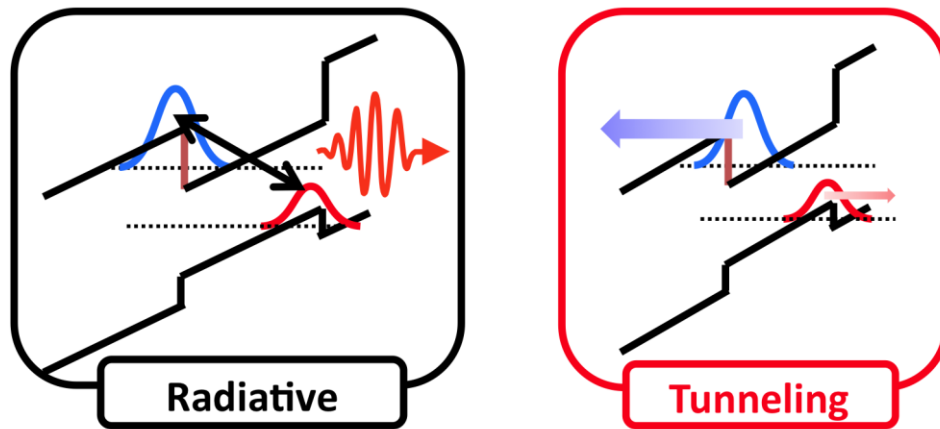
Figure 14 – Decay of the storage signal as a function of *F* compared to calculated dependence of tunneling and radiative losses.
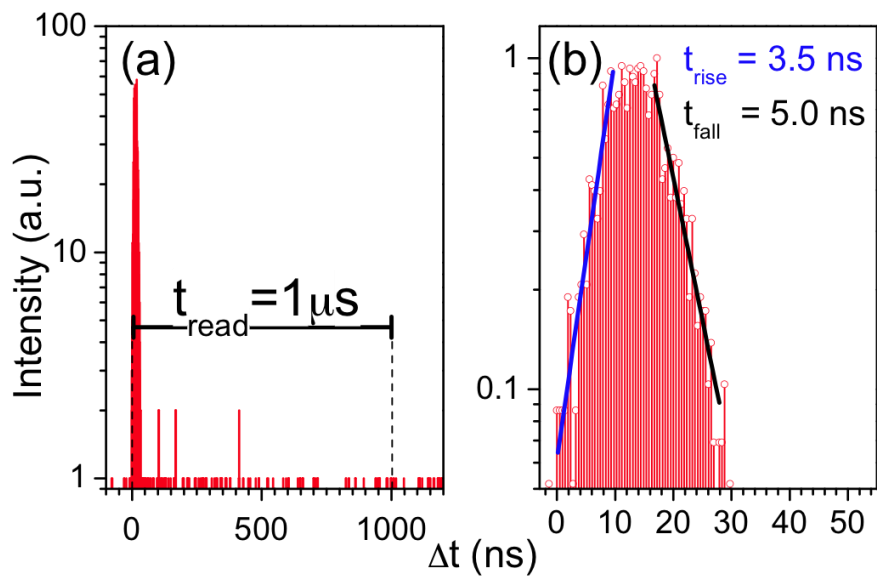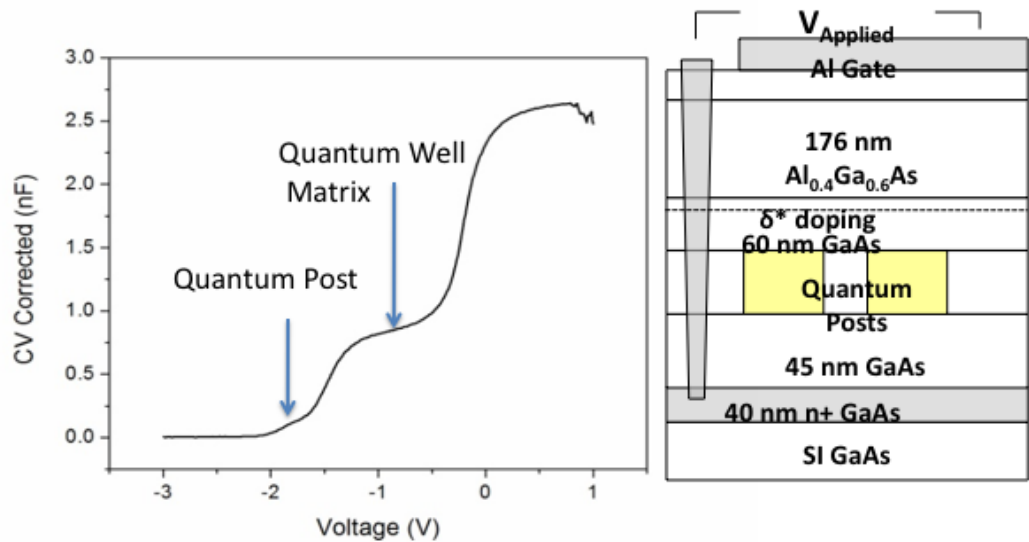
Figure 15 – Time-resolved read-out signal.

Figure 16 - Capacitance vs voltage measurements of the device structure shown schematically. The QPs height is 30 nm. The capacitance changes associated with electron loading of the quantum post and quantum well matrix are also shown. The δ-□□□ing is $n = 6.10^{11} cm^{-2}$ and $T = 10$ K. (Data courtesy of C. Morris $et\ al.$ [34])
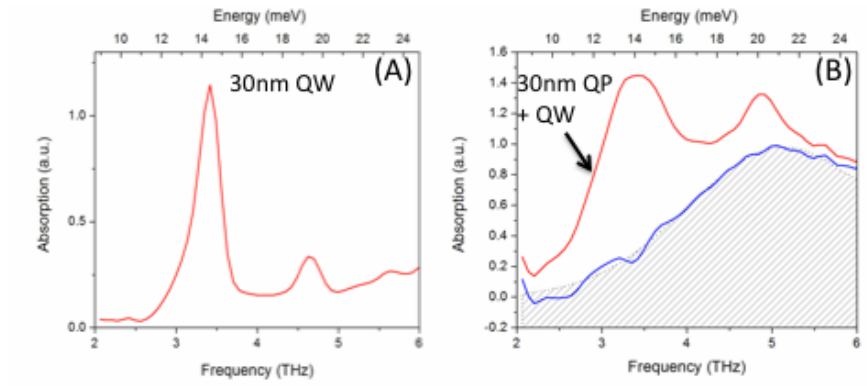
Figure 17 – Absorption spectrum of a 30nm In$_{.1}$Ga$_{.9}$As QW spectra (A) and of a 30 nm QW+QPs sample (B) at $T = 5$ K. The shaded area in (B) is obtained by deconvolution of the absorption spectrum in (A) from that in (B) and corresponds to the QPs absorption spectra (data courtesy of C. Morris *et al.* [34])